# MSEC2022-85413

# EXPERIMENTAL ANALYSIS OF METAL INERT GAS BASED WIRE ARC ADDITIVE MANUFACTURING OF ALUMINUM NANOCOMPOSITE AA7075

Mason Darnell <sup>12</sup>, Dennis Harwig <sup>2</sup>, Xun Liu <sup>12</sup>
The Ohio State University
Columbus, OH 43221

## **ABSTRACT**

This work studies Metal Inert Gas (MIG) based Wire Arc Additive Manufacturing (WAAM) for nanoparticle enhanced AA7075. MIG WAAM is important for production and large structures due to its high deposition rates compared to Tungsten Inert Gas (TIG) or powder-based AM processes. Both MIG and TIG take advantage of wire feedstock, which is more readily available than powdered metals since the welding technology has been established for decades. Powder based processes allow for more complicated geometries but take significantly more time to produce and can suffer from voids which lead to non-uniform part density. TIG is normally used in welding of aluminum because it results in fewer defects, but the TiC/TiB2 nanoparticles eliminate solidification cracking normally associated with high strength aluminum alloys during welding. Porosity is another problem faced when welding aluminum. which can be affected by many things including deposition parameters, atmosphere and even the welding equipment used. Effects of different deposition parameters have been comprehensively studied including the deposition geometry and metallurgical properties. The process is also monitored with current/voltage measurement and high-speed imaging to understand the droplet transfer mode and molten pool development. The results are used to optimize process parameters to achieve the fewest defects possible while comparing different metal transfer modes. Multi-scale characterizations will be performed to examine the porosity distribution, solidification mode and grain size through optical microscopy. Future works will explore the distribution of secondary phases, precipitates, and nanoparticles through scanning electron microscopy (SEM) as well as conducting some

mechanical testing of the as built structures such as hardness mapping and tensile tests.

Keywords: Metal Inert Gas (MIG), Wire Arc Additive Manufacturing (WAAM), Aluminum AA7075, Nanoparticles, Porosity, Welding and Joining, Materials handling, Nano-Processing

## **NOMENCLATURE**

WFS Wire Feed Speed (cm/min)
TS Travel Speed (cm/min)
I Current (A)

V Voltage (V)
HI Heat Input (J/cm)

## 1. INTRODUCTION

MIG welding is often used in place of tungsten inert gas (TIG) welding when deposition rates are more important than weld quality. The biggest difference between MIG and TIG is that the filler material carries the current in MIG welding. In MIG welding, filler materials can suffer from poor surface finish or other defects than effect the stability of the arc. Despite the drawbacks of the MIG process, it has a much higher deposition rate than TIG and powder-based processes, which makes it a very important process for industry [1][2][3]. For the additive manufacturing industry, high deposition rates are essential to further validate WAAM as a useful process. Aluminum is also an important material to consider for AM due to recent emphasis on lightweight materials [4].

MIG welding also has more freedom when it comes to building complicated structures when compared to TIG welding. Since TIG requires an off-axis wire feed system to feed the material into the arc, it would be difficult to change directions to

<sup>&</sup>lt;sup>1</sup> Contact author: darnell.52@osu.edu or liu.7054@osu.edu

<sup>&</sup>lt;sup>2</sup> Welding Engineering Program, Department of Material Science and Engineering, The Ohio State University, EJTC, 1248 Arthur Adams Drive, Columbus, OH 43221, United States of America

make certain features. This lack of flexibility in design is partly why this work focuses on the MIG process. Previous research on the nanoparticle enhanced wires have been limited to the TIG process, which is not as industry friendly in terms of deposition rates and build geometries [5][6]. The nanoparticle enhanced wire can make MIG and high strength alloys, such as 7075, more commercially viable for welding and AM by eliminating solidification cracking [7].

Nanoparticles are typically added to materials to improve properties such as tensile strength and hardness while maintaining ductility [8][9]. Nanoparticles also have the added benefit of reducing susceptibility to cracking by changing the solidification mode of aluminum alloys, from columnar dendritic to equiaxed globular/dendritic depending on the type of nanoparticle used [7]. This change in solidification mode comes from heterogeneous nucleation, due to the high temperature stability of the nanoparticles included. Equiaxed grains are favorable to prevent cracking since dendrites trap liquid between them during solidification and will more easily propagate a crack/tear. The nanoparticles also modify the nature of the secondary phases, with dendritic solidification the secondary phase will form continuously between the dendrites, whereas with heterogeneous nucleation creating equiaxed grains the secondary phase is discontinuous. The discontinuous nature of the secondary phase plays a large role in reducing crack susceptibility.

Alloying elements extend the solidification temperature range compared to pure Al, therefore alloys such as 7075 will have a much larger solidification temperature range compared to 3xxx, 5xxx and 6xxx series aluminum for example [10]. The amount and type of alloying elements in 7075 strengthen the alloy more than other series due to both solid solution and precipitation strengthening [11][12], adding to cracking susceptibility by providing higher self-restraint upon cooling/solidifying which also lead to shrinkage porosity. Shrinkage porosity can be identified by the non-uniform shape, opposed to hydrogen porosity which is always round/spherical. Nanoparticles eliminate cracking by providing smaller equiaxed grains and more tortuous crack path. Since no cracking was observed in any of the walls made for this study, faster builds can be completed since convention is to let welds cool for longer time than this work to avoid cracking. Letting the welds cool down will reduce the interpass temperature and effectively increase the cooling rate, with an increased cooling rate the liquid films between grains will have less time to separate and nucleate/propogate cracks. Alloying elements, such as zinc, can also be vaporized during welding and create additional porosity [13]. It can be seen from the work of Li et al. [14] that the deposit contains less zinc than the wire used. This zinc loss would likely be less prevalent in TIG based processes where the droplet is not transferred directly through the arc.

Hydrogen absorbed during liquid phase at elevated temperature is the main source of porosity in aluminum welding. To reduce porosity, some researchers have explored higher interpass temperatures that would let hydrogen float out during solidification [15]. There are possible compositional effects of

certain alloys containing Mg & Cu on hydrogen absorption and threshold for pore nucleation/growth [16]. P. Legait also suggests that faster cooling rates could help prevent pores from forming in the first place by giving less time for diffusion/growth, future work will include trials of lower interpass temperatures. Waiting longer between welds for faster cooling rates gives oxide layer more time to form, in theory will negatively impact arc stability and allow for more large pores concentrated at the fusion boundaries of each layer. Nanoparticles act as heterogenous nucleation sites for both grains and porosity, better wetting of particle to matrix would reduce porosity [17]. Porosity distribution suggests most of porosity is either shrinkage induced, or nanoparticle induced due to size.

Choosing the correct waveform for the DC MIG process is of great importance to reduce porosity and help arc stability. MIG power supplies typically utilize DC current, however AC options are available and have benefits over DC power supplies [18]. There are multiple ways to increase the effectiveness of DC waveforms through manipulating pulse frequency and current. Changing pulse frequency can affect overall part density by lowering porosity, and can create a smoother surface finish on top of the deposited layers [19][20][21]. Direct current electrode positive polarity (DCEP) also provides cathodic cleaning due to the direction of current flow breaking up oxides on the base metal [22]. Pulse frequency will impact the effectiveness of the cleaning action, but also have other implications depending on the material and current ranges used. Waveform parameters in this study were kept at the recommended values based on the power supply.

Based on the recommended values from the power supply listed in the materials and methods section below, a predominantly pulsed globular transfer mode was achieved when compared to existing literature on pulsed waveforms [23][24]. Globular transfer is notably characterized by the droplet being larger than the diameter of the wire, which is the case for this study. Globular transfer in non-pulse waveforms tend to produce significantly larger drops, and less stable detachment. Spray transfer is typically achieved with a higher arc length than that of globular transfer, and produces droplets less than the diameter of the wire. Pulsed waveforms help stabilize the detachment of the drop from the wire with base and peak currents, where the peak current is used to melt the wire and the transition between peak and base current is used to help detach the droplet [25]. Most literature regarding pulsed waveforms recommends achieving one drop per pulse, which was found to be the case on average for this study [24][25].

Wire surfaces can also contain contaminants in the form of oil, grease, dirt or moisture. Moisture on the wire surface can increase porosity, and other contaminants combined with alloying elements such as magnesium/zinc can create a surface scale with colors ranging from brown to black. The effect of the surface scale deposited after each layer was found to be negligible [26]. Interpass cleaning with the wire brush was found to have a negative impact on porosity through experimentation,

therefore was not conducted for the samples presented in this paper.

## 2. MATERIALS AND METHODS

#### 2.1 Materials

The AA7075 Nanocomposite wire is manufactured by Metali, which contains TiB<sub>2</sub> nanoparticles with wire diameter of 1.2mm. This is different from the works of Sokoluk et al and Orepeza et al [5][6], where the welding wire contains the TiC nanoparticles, and the wire diameter is 3.2 mm.

Substrate used is AA2219-T87 in rolled plate condition, which is a commonly used aluminum alloy for structural purposes Due to deposition size and depth of penetration, there is likely no dilution after two or three beads. Further chemical composition analysis and calculations are needed to confirm this.

# 2.2 Welding Methods

Preparation of the base plate follows standard practices for aluminum welding. The base plate is first cleaned mechanically with an aggressive grinding disk to remove the passive oxide layer that inhibits formation of the welding arc and promotes porosity formation. Milling of the base plate was also evaluated as an alternative approach for deposit surface preparation. The building results in terms of porosity is similar to the grinding approach, which was chosen for the rest of the experiments. After grinding, chemical cleaning with acetone is then used to remove any other contaminants that would cause additional instability of the arc or porosity. Due to the nature of welding consumables manufacturing, there are many possible defects that vary from batch to batch and from manufacturer to manufacturer [26].

The 6-axis OTC robot with the OTC Welbee P500L power supply was used to build the additive walls. Welding was conducted using DCEP polarity, which focuses heating onto the wire instead of the substrate. Figure 1 below depicts the DC double pulse waveform used during the deposition process. Compared with single pulse or regular DC waveforms, the double pulse waveform produces the least amount of deposition porosities in the initial studies. A nozzle to work distance of 12 mm was used, which results in a contact tip to work distance of 19 mm. The resultant average current, voltage, heat input and layer height are recorded in Table 1 below. Regarding the average layer height per sample, the first two layers were always taller and thinner than the subsequent beads due to interpass temperature. Current is controlled by setting wire feed speed (WFS) and voltage was controlled through a "trim" factor (from -100 to +100). Trim was adjusted after running trials to find values that resulted in desired voltage for each WFS. A voltage of roughly 20V was used for initial trials, and upon further investigation with high-speed imaging was found to produce a globular transfer mode with this material. Some instances of short circuiting and spray transfer were observed through both data acquisition for current/voltage waveforms and through high-speed imaging respectively. Each instance of short circuiting will correlate to increased porosity in the sample at that location along the weld length due to instability associated with the short circuit transfer mode.

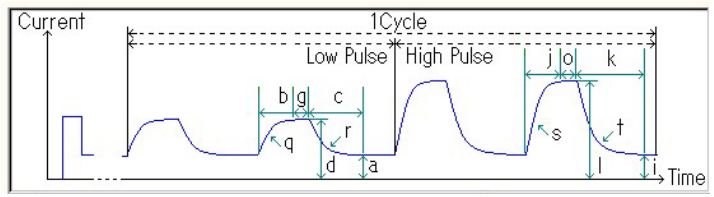


**Figure 1:** Waveform from OTC power supply depicting the double pulse waveform with two different peak currents (Pulse Wave). All other parameters related to pulse frequency and base current are the same for each low and high pulse regime.

**Table 1:** Resultant average voltage, current and layer height from range of deposition parameters corresponding to the parameter combinations from the DOE structure [Table 3]. Build parameters correlate to DOE #. A, V, HI and Height are average values for each 10 bead wall.

| Average Resultant Current, Voltage, Heat Input and Layer Height for DOE Parameters |     |      |           |             |  |
|--|-----|------|-----------|-------------|--|
| DOE#   | A   | V    | HI (J/cm) | Height (mm) |  |
| 211  | 165 | 20.7 | 3401      | 1.60        |  |
| 212  | 160 | 20.2 | 4371      | 1.90        |  |
| 213  | 160 | 19.9 | 5324      | 2.21        |  |
| 221  | 181 | 20.2 | 3228      | 1.68        |  |
| 222  | 184 | 19.9 | 4322      | 2.08        |  |
| 223  | 183 | 20.2 | 5402      | 2.18        |  |
| 231  | 200 | 20.3 | 3212      | 1.68        |  |
| 232  | 204 | 20.6 | 4414      | 1.94        |  |
| 233  | 203 | 20.7 | 5473      | 2.23        |  |

An inter-pass temperature upper limit of 150°F was kept to prevent degradation of the geometry from too much heat. The interpass temperature never dropped below roughly 115°F before the next weld and was on average closer to 130°F past the third bead. Too high an interpass temperature will create a "mushroom" effect that will envelope the previous beads and not result in a proper wall. Keeping the inter-pass temperature above room temperature should help to decrease porosity by giving the hydrogen/other gas bubbles time to escape during cooling [15]. Pure argon shielding gas was used, the main gas nozzle had a flow rate of 40 CFH. A trail shield is also employed to enhance shielding of the weld by providing more inert gas over the solidifying metal and helps with porosity reduction. The trail shield required a slightly higher flow rate to operate successfully and is set at 45 CFH.

# 2.3 Experimental Methodology

Analysis of the nanoparticle enhanced AA7075 welding wire involves systematically identifying the relevant welding parameters believed to affect the process stability. For the initial

work, only 9 of the possible 27 parameter combinations were tested due to time [Table 3]. Voltage of 18V was found to produce significantly more porosity than 20V, while 22 V was found to be too similar to 20V results in terms of droplet transfer mode. Table 2 shows the original design of experiment matrix for parameter optimization based on preliminary testing.

**Table 2:** DOE Levels and Parameters.

| DOE Levels and Parameters |     |      |      |  |
|---------------------------|-----|------|------|--|
| Level                     | 1   | 2    | 3    |  |
| Voltage                   | ~18 | ~20  | ~22  |  |
| WFS                       | 889 | 1016 | 1143 |  |
| WFS/TS                    | 15  | 20   | 25   |  |

**Table 3:** DOE Table Structure for parameter combinations

explored in this work.

| in this work.       |         |     |        |  |  |
|---------------------|---------|-----|--------|--|--|
| DOE Table Structure |         |     |        |  |  |
| trial no.           | Voltage | WFS | WFS/TS |  |  |
| 1                   | 2       | 1   | 1      |  |  |
| 2                   | 2       | 1   | 2      |  |  |
| 3                   | 2       | 1   | 3      |  |  |
| 4                   | 2       | 2   | 1      |  |  |
| 5                   | 2       | 2   | 2      |  |  |
| 6                   | 2       | 2   | 3      |  |  |
| 7                   | 2       | 3   | 1      |  |  |
| 8                   | 2       | 3   | 2      |  |  |
| 9                   | 2       | 3   | 3      |  |  |

The heat input in table 1 above was calculated using the following formula (1) to evaluate the effect of process parameters on energy input during welding. This energy input is based on average current and voltage, but instantaneous values could be calculated using current and voltage waveforms obtained form DAQ.

Heat Input = 
$$\frac{I*V*60(sec.)}{TS} \left[ \frac{J}{cm} \right]$$
 [27] (1)

Using a data acquisition system for current/voltage during the process, and high-speed imaging allows for tuning of the parameters to avoid short circuiting and other unstable characteristics. For the purposes of this study, default parameters from the power supply were used for a given WFS, and voltage was adjusted to achieve values listed in DOE matrix. Details of the results of DAQ and high-speed imaging will be explored in the results section. The camera used is a Photron SA-X2 with a 1x magnification lens. Filming was conducted at 6000 frames per second to capture the frequency of the pulse waveform, which was 250 Hz for all parameter combinations.

# 2.4 Analysis Techniques

All samples are analyzed in the as-welded condition. The metallurgical samples are sectioned normal to the building direction, and prepared following standard grinding and polishing procedure. The samples are etched with Barker's reagent, at roughly 25V for 2.5 minutes. This etchant is capable of revealing the secondary phases and the majority of grain boundaries, however certain grain boundaries without much secondary phase were less clear. Quantification of grain structure from macrographs was initially conducted with ImageJ and the less identifiable grain boundaries are manually marked up for program thresholding. Images were taken at the 1um polishing step to reveal the full range of porosity sizes present in the sample.

#### 3. RESULTS AND DISCUSSION

## 3.1 Porosity Analysis

The porosity measured through optical microscopy is not as reliable as other methods such as computed tomography (CT scanning) as it is limited to a single cross section along the length of the weld. The waveform viewed from the DAQ in Figure 3 shows an example of voltage instability from a weld in the DOE table and can be correlated to higher levels of porosity along the length of the weld. Some of the porosity trends seem inconsistent when analyzed this way, so in the future CT scanning will be performed to get a 3D volume fraction of porosity. All parameter combinations had instances of short circuiting, with parameter combination 232 having the least. Table 4 contains measured area fractions of porosity for each parameter combination. Figure 2 shows the cross section of sample 232 polished at 1um. Due to time constraints only one cross section was taken per sample, but multiple cross sections along the length of each sample would also ensure better accuracy. Parameter combination 232 seems to achieve the minimal amount of porosity according to the cross-sectional analysis, most likely due to the synergy of the WFS and pulse frequency. The WFS determines current/melting rate and can be matched with an optimal pulse frequency to ensure stability and the recommended one drop per pulse [24][25]. Since WFS/current determine melting rate, a higher WFS/current can handle a higher pulse frequency without instability. If a lower WFS/current value is used, a lower pulse frequency should be applied. The default parameters from the power supply for all parameter combinations resulted in a pulse frequency of 250 Hz.

The formation of porosity in these samples was caused by instability in the welding process and heterogeneous nucleation from nanoparticles which are stable at the elevated temperatures during welding [16][17]. Large pores are from entrapped atmospheric gas pulled into the molten material by are instability. Small pores could be explained by hydrogen bubbles nucleating from the surface of TiB2 particles/clusters or whetting issues of the aluminum matrix to TiB2 particles/clusters. Most pores appear to be round and spherical in nature indicating hydrogen porosity, but instances of shrinkage porosity were observed and found to occur mostly at grain

boundaries where there was insufficient amounts of liquid film to fill the resultant void. Shrinkage pores ranged from 25-100% the size of grains in locations 1 and 3. When comparing the material used in this study to those examined in the work mentioned previously [26], the surface finish contains significantly more defects such as scratches and dimples. The surface defects present can likely be explained by the increased strength of the already strong AA7075 due to the nanoparticles. The increased strength would make the wire drawing process more difficult and result in more wear on the tooling.

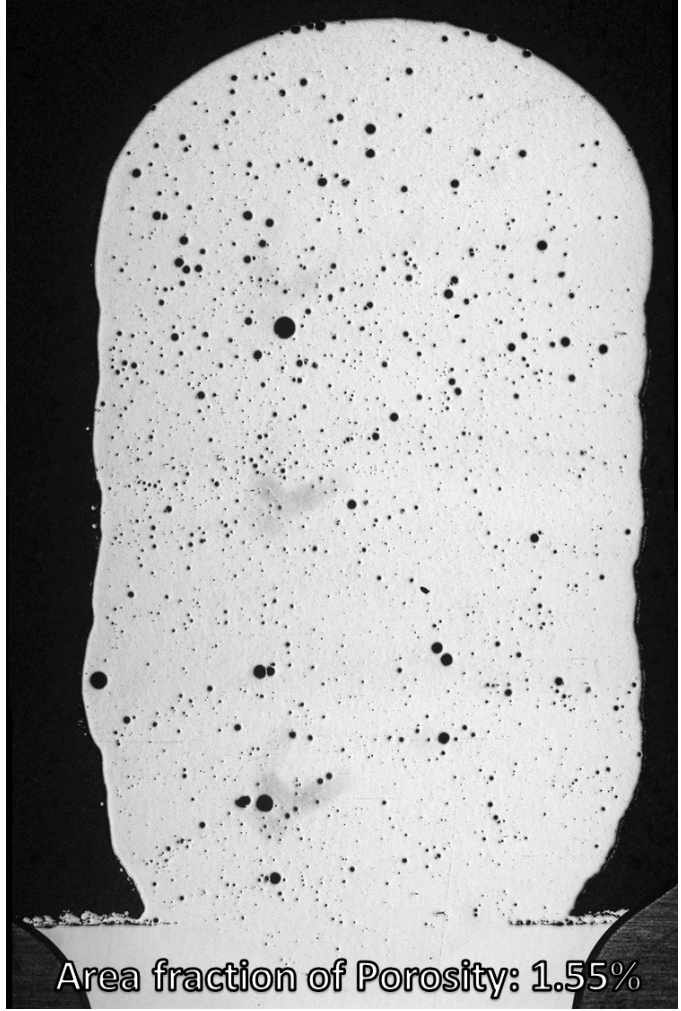


**Figure 2:** Polished image with area fraction of porosity. Sample [232]

**Table 4:** Percent porosity analyzed through optical microscopy cross section, polished at 1um.

| Porosity Area Fraction |            |  |
|------------------------|------------|--|
| DOE #                  | % Porosity |  |
| 211                    | 9.415%     |  |
| 212                    | 9.683%     |  |
| 213                    | 8.320%     |  |
| 221                    | 7.649%     |  |
| 222                    | 8.550%     |  |
| 223                    | 4.356%     |  |
| 231                    | 7.965%     |  |
| 232                    | 1.548%     |  |
| 233                    | 4.486%     |  |

Figure 3 depicts an example of short circuiting as detected by the data acquisition, right after the 9.24 second mark. Figure 4 shows the pulsed-globular transfer mode achieved with the voltage obtained during this study with labels of the relevant parts of the images. One drop per pulse was achieved on average, with instances of unstable spray transfer occurring after the main drop had transferred. This unstable spray could likely be explained by the ligament attaching the drop to the wire also detaching from the wire after the main drop transfers.

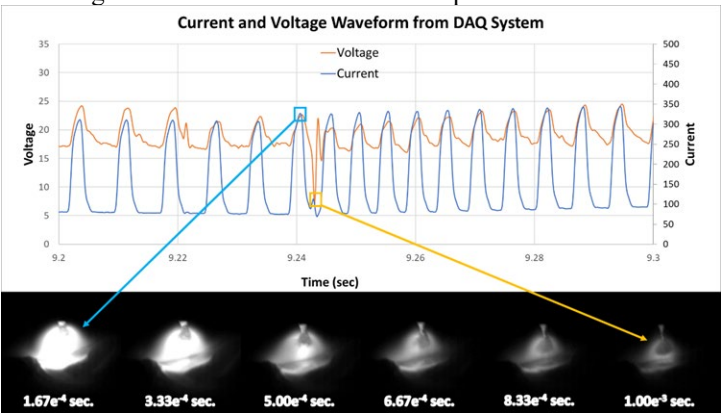


**Figure 3:** Waveform for current and voltage from DAQ system coupled with locations of peak/base current, with the base current example showing short circuiting/instability due to ligament of molten metal connecting the drop to the wire during transfer.

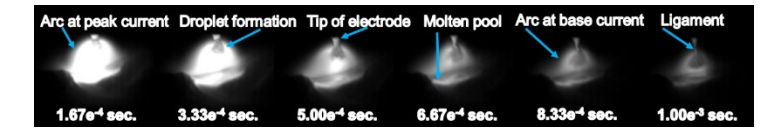


**Figure 4:** Depicting instance of short circuiting/voltage instability caused by ligament attaching globular drop at the end of a pulse cycle.

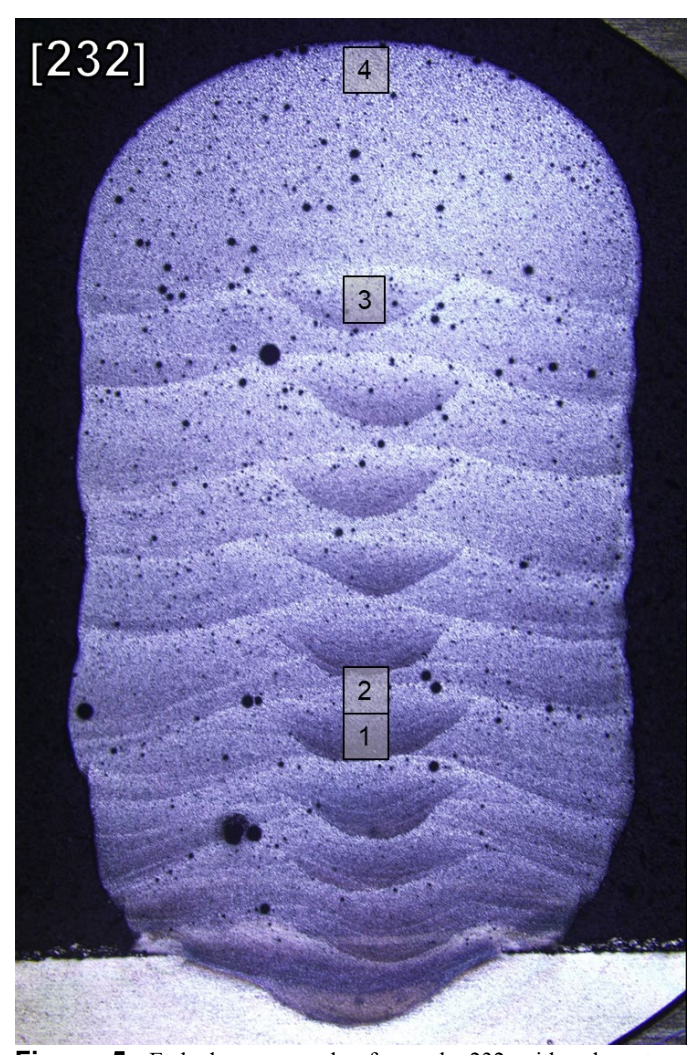
Porosity is almost always a bad sign when welding or conducting additive manufacturing. Large pores are much worse for properties than small ones owing to the amount of material that is lost. However, small pores have the possibility of increasing fatigue life by acting as crack arrestors [28]. The paper by P. Ferro explores the idea of putting holes near sites where fatigue cracks would be expected to propagate. All builds in this study had similar porosity distributions consisting of mainly small pores approximately 2-4 times the size of the grains concentrated near the fusion boundaries and geometry seen on the sides of the wall. The idea that these holes would increase fatigue life has not yet been explored in metals, as the previous study used resin printed by stereolithography.

# 3.2 Grain Size Analysis

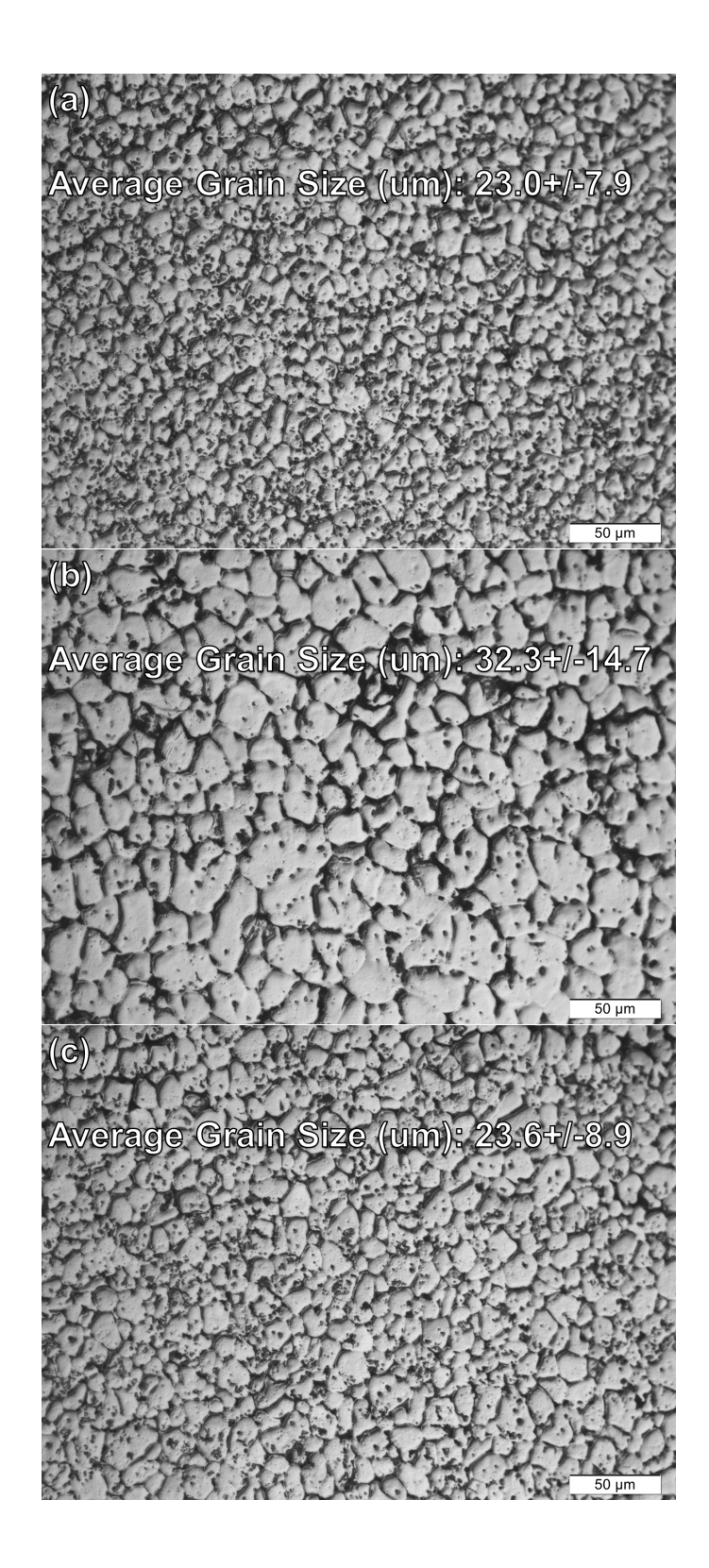
Grain size within each deposition layer are affected by local cooling rates associated with the WAAM process, similar results are found in the paper by S. Li [14]. Higher cooling rates based on conduction occur at the bottom of the beads compared to lower cooling rates from convection on the top and sides of the bead. Deposition size and heat input will influence local cooling rates, but despite different heat inputs, all samples and weld beads display similar trends of porosity and grain size distributions. Grain sizes near the bottom of each layer are between 25-50% smaller than the middle or top of the bead (Figures 5, 6 & 7). Another important aspect related to additive manufacturing is that all the beads except the topmost bead are partially remelted and reheated. This single instance of remelting causes the fusion boundary to be located near the middle and top regions of the previous bead based on distance from the center of the wall, and the cyclical reheating during subsequent layer deposition should cause the grains to grow in locations 1 and 2. Grain growth is not observed in location 1 as expected, and location 2 has grain sizes similar to the halfway point between location 3 and 4. Grain size distributions for each set of parameters are similar and no trends are discernable other than grain size varying based on location within the sample (Figure 7). Location 3 is expected to have a larger grain size than location 1 due to reheating from subsequent depositions, but no such grain growth is observed. It is likely that the nanoparticles pin the grain boundaries and prevent grain growth in location 1.

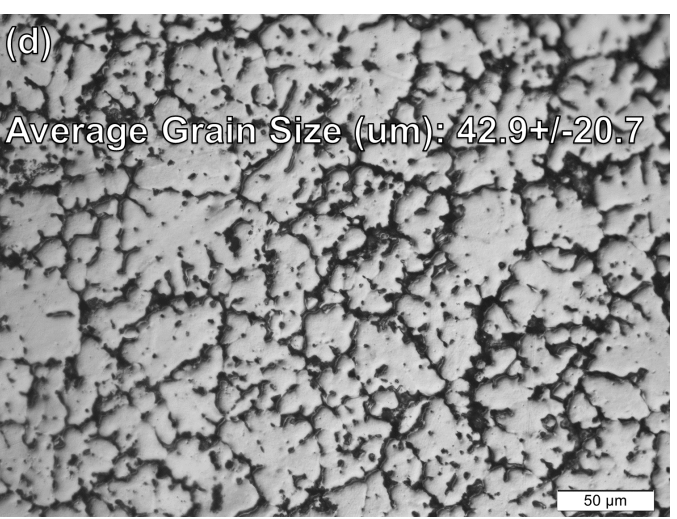
Another important quality of the nanoparticle enhanced material is the change from columnar dendritic solidification structures to equiaxed grains [5][6][9], location 4 from Figure 5 and Figure 6 (d) show equiaxed dendrites. The nanoparticles provide heterogeneous nucleation sites but do not fully suppress the dendritic features normally associated with aluminum solidification [7]. The equiaxed dendritic and globular grains form due to heterogeneous nucleation and epitaxial growth from the nanoparticles/clusters. The micrograph depicted in Figure 5 (d) is of the top part of the topmost bead on the wall and its microstructure is quite different than the other examples of the same sample. The other micrographs depict equiaxed, globular grains while the top of the top bead more closely resembles a cast microstructure of 7075 [7][29]. The top of the top bead resembling cast microstructure in the form of rosette shaped

grains suggests that reheating of the previous beads transforms the somewhat dendritic structure into more equiaxed shapes in the middle bead top section, or that the region containing rosette shaped grains is remelted and eliminated entirely from all but the topmost bead. It was observed that a transition between equiaxed dendrites and equiaxed globular grains occurs roughly halfway between location 4 and 3 in the top bead. This transition is expected to occur in each bead but the evidence of equiaxed dendrites is eliminated by the reheating process, which is believed to straighten out the grain boundaries via grain boundary migration. The nanoparticles pin the grain boundaries enough to prevent grain growth, but still allow for some evolution of the grain morphology.

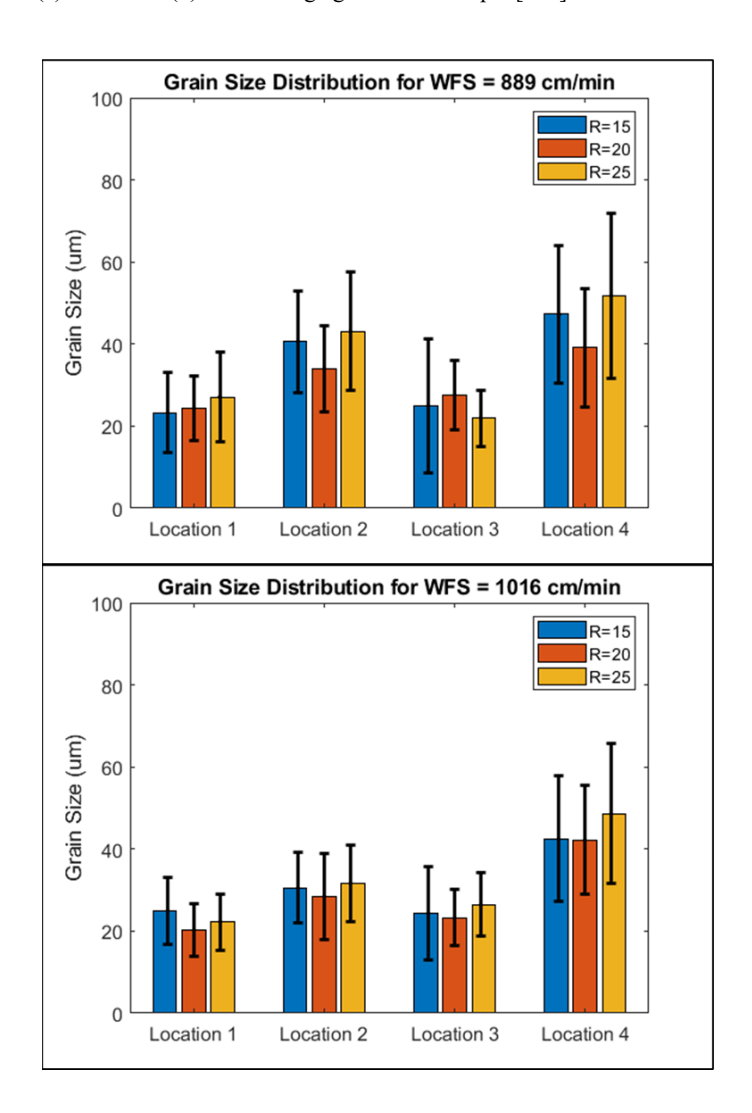


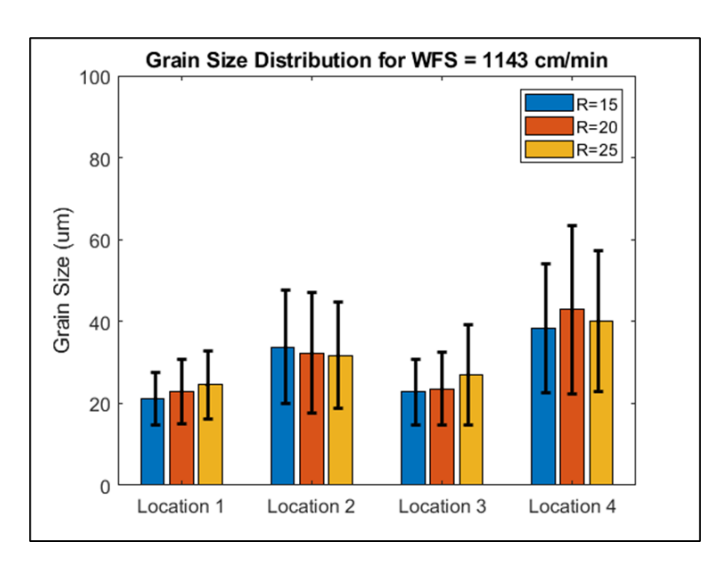
**Figure 5:** Etched macrograph of sample 232 with relevant locations marked for grain size measurements in Figure 6.





**Figure 6:** Etched micrographs within regions of interest from etched macrograph (Figure #): location 1 (a) location 2 (b) location 3 (c) location 4 (d) with average grain size. Sample [232]

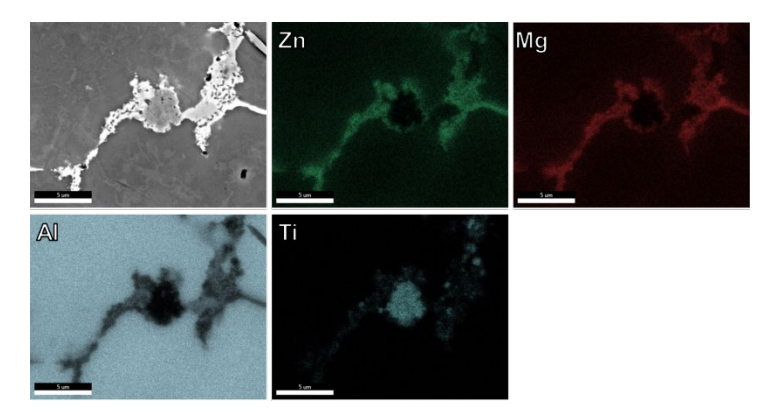




**Figure 7:** Bar charts with standard deviation plotted as error bars for each WFS explored, locations are compared by deposition size (WFS/TS).

# 3.3 Nanoparticle Clusters in SEM

Another feature of interest that is evident in the micrographs Figure (a-d) is size/location 6 the of the precipitates/nanoparticle clusters. Compared TiC nanoparticles studied in the work of Sokuluk et al. [5][6] the TiB2 particles have worse dispersion capabilities and are more likely to agglomerate [7]. Since MIG welding based AM involves transferring material through the welding arc, it is expected that the nanoparticles would be exposed to temperatures higher than those of the TIG welding trials done previously. Clusters/particles tend to concentrate along grain boundaries and within the secondary phase due to the particles being pushed by the solidification front as shown in figure 8. The TiB2 particles have higher solubility in the secondary phase than in the aluminum matrix, which also explains why the clusters are not found within the grain interiors as often.



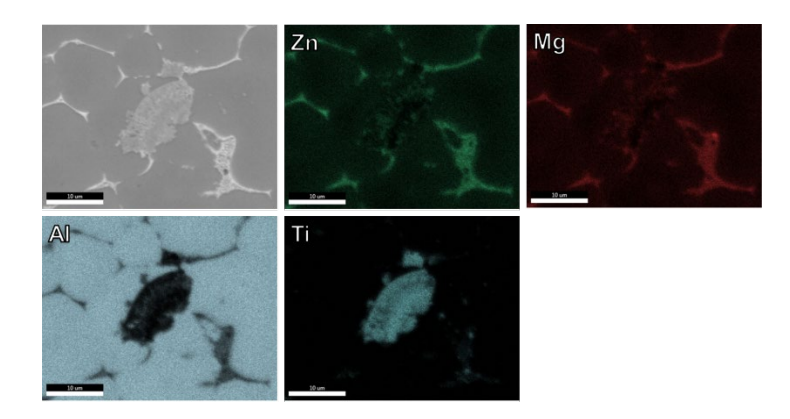


**Figure 8:** SEM and EDS map of TiB2 agglomerations in top (top figure) and bottom (bottom figure) of additive wall.

#### 4. CONCLUSION

Of the nine different parameter combinations explored, parameter set 232 resulted in the least amount of porosity. Based on data acquisition and high-speed imaging it seems that this parameter set is the most stable combination of voltage, current, wire feed speed and travel speed for the nanoparticle enhanced AA7075. All parameter sets regardless of heat input display similar trends in grain size throughout the wall and within each bead. Porosity size distributions are also similar across all parameter sets, where there are few large pores and many small pores. Measurements taken have an inherent error based on where the micrograph was taken, and which grains were able to be detected through analysis.

## 4.1 Future Work

- SEM analysis of secondary phase, nanoparticle clusters and EBSD
- CT scan data for volume fraction of porosity
- Mechanical testing including hardness maps and tensile tests
- Data acquisition to acquire actual cooling rates, both locally and macroscopically
- Heat treatments similar to those used for nominal AA7075 compositions for comparison

## **ACKNOWLEDGEMENTS**

This work was supported by National Science Foundation CMMI AM Award # 2044526: CAREER: Ultrasonically Assisted Wire Arc Additive Manufacturing of Metal Matrix Nanocomposites for High-strength, Lightweight Structures.

#### **REFERENCES**

- [1] D. Herzog, Additive manufacturing of metals, 2016
- [2] D. Ding, Wire-feed additive manufacturing of metal components: technologies, developments and future interests, 2015
- [3] T. Rodrigues, Current Status and Perspectives on Wire and Arc Additive Manufacturing (WAAM), 2019

- [4] K. Derekar, A review of wire arc additive manufacturing and advances in wire arc additive manufacturing of aluminium, 2018
- [5] M. Sokuluk, Nanoparticle-enabled phase control for arc welding of unweldable aluminum alloy 7075, 2019
- [6] D. Orepeza, Welding and additive manufacturing with nanoparticle-enhanced aluminum 7075 wire, 2020
- [7] M. Sokuluk, Nanoparticles Enabled Mechanism for Hot Cracking Elimination in Aluminum Alloys, 2021
- [8] X. Li, Theoretical and experimental study on ultrasonic dispersion of nanoparticles for strengthening cast Aluminum Alloy A356, 2008
- [9] M. Zuo, Microstructure Control and Performance Evolution of Aluminum Alloy 7075 by Nano-Treating, 2019
- [10] J. Lippold, Welding Metallurgy and Weldability, 2014
- [11] R. Ambriz, Mechanical Behavior of Precipitation Hardened Aluminum Alloys Welds, 2014
- [12] J.R. Davis, Alloying: Understanding the Basics, 2001
- [13] P. Legait, Formation and Distribution of Porosity in Al-Si Welds, 2005
- [14] S. Li, Microstructures and mechanical properties of Al–Zn–Mg aluminium alloy samples produced by wire + arc additive manufacturing, 2020
- [15] K. Derekar, Influence of Interpass Temperature on Wire Arc Additive Manufacturing (WAAM) of Aluminium Alloy Components, 2019
- [16] P. Legait, Formation and Distribution of Porosity in Al-Si Welds, 2005
- [17] M. Mazur, Porosity in aluminum welds, 1992
- [18] D. Harwig, Arc Behavior and Melting Rate in the VP-GMAW Process, 2006
- [19] D. Wang, Reducing Porosity and Refining Grains for Arc Additive Manufacturing Aluminum Alloy by Adjusting Arc Pulse Frequency and Current, 2018
- [20] C. Mended da Silva, The influence of double pulse on porosity formation in aluminum GMAW, 2005
- [21] P. Praveen, Meeting challenges in welding of aluminum alloys through pulse gas metal arc welding, 2005
- [22] R. Sarrafi, Cathodic Cleaning of Oxides from Aluminum Surface by Variable-Polarity Arc, 2010
- [23] Y.S. Kim, Metal Transfer in Pulsed Current Gas Metal Arc Welding, 1993
- [24] S. Subramaniam, Droplet Transfer in Pulsed Gas Metal Arc Welding of Aluminum, 1998
- [25] P.K. Palani, Selection of Parameters of Pulsed Current Gas Metal Arc Welding, 2006
- [26] E.N. Ryan, Relationship between porosity and surface deposit coverage for wire and arc additive manufactured aluminium alloy 2319, 2018
- [27] AWS D1.1 section 6.8.5.1
- [28] P. Ferro, Crack arresters design for fatigue strength improvement of additively manufactured components, 2020
- [29] X. Li, Evaluation of the thixoformability of AA7004 and AA7075 alloys, 2008